PHYSICAL REVIEW E **72**, 041924 (2005)

Comparison of density functional theory and simulation of fluid bilayers

Amalie L. Frischknecht and Laura J. Douglas Frink*
Sandia National Laboratories, Albuquerque, New Mexico 87185, USA

(Received 18 October 2004; revised manuscript received 7 July 2005; published 25 October 2005)

We compare results of classical density functional theory (DFT) to molecular dynamics (MD) simulations of coarse-grained models of lipids in solvent. We find that the DFT captures the liquid structure of coarse-grained lipids both near surfaces and in bilayers adequately. In contrast we find that the MD simulations do not predict ordering in bilayers as is observed in low temperature DFT calculations. The mechanical properties of the fluid DFT bilayers are qualitatively similar to those of the MD bilayers; in particular the shapes of the lateral stress profiles are similar. Values of the area compressibility modulus are in reasonable agreement with previous work on coarse-grained lipids.

DOI: 10.1103/PhysRevE.72.041924 PACS number(s): 87.16.Dg, 87.15.Aa, 87.14.Cc

I. INTRODUCTION

Lipid bilayer membranes play important functional roles in biological systems. A detailed understanding of their structure and mechanical properties can help to elucidate the behavior of lipid domains and membrane proteins. Since the biologically relevant phase of lipid bilayers is the disordered, fluid phase, it is difficult to extract detailed information on bilayer properties from experiment. Computer simulations have played a complementary role in obtaining and understanding this information. However, atomistic simulations are limited to space and time scales that are too short to capture many interesting processes and features of lipid bilayers, such as the formation of lipid domains or rafts, the interactions of transmembrane proteins, and membrane fusion. As a result, there has been increasing interest in developing more coarse-grained models to describe lipid membranes [1].

These models have taken a variety of forms. The shapes and internal degrees of freedom of the model lipids vary, from rigid spherocylinders or rigid chains of beads with no internal degrees of freedom, to more flexible chains of spherical beads. Both lattice and off-lattice simulations have been performed on coarse-grained lipid models. Techniques include molecular dynamics (MD), Monte Carlo, and dissipative particle dynamics (DPD). Recently, efforts have been made to build united-atom-type models based on atomistic force fields, in order to obtain coarse-grained models that can give relatively quantitative results [2,3].

A more generic coarse-grained model that maintains the internal degrees of freedom of the lipids is that introduced (for lipid bilayers) by Goetz and Lipowsky [4]. Their model consists of chains of spherical interaction sites, which interact through Lennard-Jones interactions, a bonding potential for bonded neighbors, and angle potentials. This model has been used in both MD and DPD simulations, and has been shown to self-assemble from random initial conditions into bilayers. The model has also been used to obtain bilayer properties such as the elastic constants, to study the liquid to gel phase transition, and to simulate vesicle fusion [4–8].

These kinds of spherical interaction site models can also be treated using classical density functional theory (DFT). In the preceding paper ([9], hereafter referred to as paper I), we presented a theoretical framework for the equilibrium properties of lipid bilayers that treats the lipid chains in a coarse-grained molecular fashion using a DFT approach previously developed for inhomogeneous and self-assembling polymers [10–15]. In paper I we presented bilayer structures, an analysis of bilayer hydration, and phase diagrams based on one-dimensional morphologies for the model system.

Here we explore the accuracy of the DFT approach by comparison to MD simulations of flexible chain lipids. To our knowledge, all previous MD simulations of coarse-grained lipids in the literature [3–5,7,8] have treated the lipid tails as semiflexible, by including an angular bending potential between monomers. Since our DFT treats the lipid tails as freely jointed, random walks, we need to compare to MD simulations on flexible-tail lipids. Thus in this paper we perform MD simulations on the model lipid system introduced in paper I. Section II provides a summary of the DFT and details of the MD simulations, Sec. III presents calculations of lipids and solvated lipids at surfaces along with a discussion of the solvent model, Sec. IV compares bilayer structures predicted from the theory to MD calculations, and finally Sec. V compares physical properties of the membrane to predictions from the DFT. Generally we show that the agreement between the methods is adequate for fluid bilayers, with room for improvement in the quality of the solvent model.

II. METHODS

A. Model system

Our coarse-grained lipid model (see paper I for details) consists of a freely jointed chain of tangent sites, with a head group and two tails. The tails consist of eight interaction sites or "beads" while the head group is composed of two larger beads. This 8-2-8 model roughly groups two CH_2 groups per bead, and the ratio of head to tail bead diameters ($\sigma_h/\sigma_t=1.44$) was chosen on the basis of simple packing arguments

---

*Corresponding author. Electronic address: ljfrink@sandia.gov

that predict lamellar or bilayer assemblies. The model also includes a single site solvent.

The interactions between different site types in the model are based on Lennard-Jones (LJ) interactions, with the various energetic constants set to bias the system toward self-assembly. Specifically, the interaction potentials are

$$u_{\alpha\beta}(r) = u^{LJ}_{\alpha\beta}(r) - u^{LJ}_{\alpha\beta}(r_c), \tag{1}$$

$$u^{LJ}_{\alpha\beta}(r) = \frac{4\epsilon_{\alpha\beta}}{kT}\left[\left(\frac{\sigma_{\alpha\beta}}{r}\right)^{12} - \left(\frac{\sigma_{\alpha\beta}}{r}\right)^{6}\right], \tag{2}$$

where r_c is the cutoff distance where the potential goes to zero, k is Boltzmann's constant, and T is the temperature. In addition to the lipid molecules, the model has a single site solvent with diameter $\sigma_s = \sigma_t \equiv \sigma = 1$. The cross terms in the bead diameters are found from the usual Berthelot scaling rules, so that $\sigma_{\alpha\beta} = 0.5(\sigma_\alpha + \sigma_\beta)$. The tail-solvent and tail-head interactions are purely repulsive with $r_c = 2^{1/6}\sigma_{ts}$ and $r_c = 2^{1/6}\sigma_{th}$, respectively. Solvent-solvent, solvent-head, head-head, and tail-tail interactions are all uniformly attractive with a cutoff of $r_c = 3.5\sigma$. Finally, we set all of $\epsilon_{\alpha\beta} \equiv \epsilon = 1$. This combination of parameters allows for a self-assembling bilayer to form. We will report all lengths in units of σ and energies in units of ϵ/kT.

B. DFT calculations

The DFT is a mean-field theory for inhomogeneous chain liquids, based on the DFT of Chandler, McCoy, and Singer (CMS) [10–12]. The properties of the bulk system are calculated using the polymer reference interaction site model (PRISM) theory [16,17]. The direct correlation functions $c_{\alpha\beta}(r)$ for the effective interactions between sites in the bulk fluid are obtained from this theory and used as an input to the CMS DFT.

The DFT calculations are done in the grand canonical ensemble where the state variables are the volume V, the temperature T, and the chemical potentials of the solvent and lipid species, μ_s and μ_L, respectively. In our formulation, μ_s and μ_L are manipulated via a total site density ρ_b and the solvent number fraction x_s in a bulk reservoir fluid in equilibrium with the fluid in the computational domain. Given a thermodynamic state, the calculations produce density profiles $\rho_t(x)$, $\rho_h(x)$, and $\rho_s(x)$, for tail beads, head beads, and solvent, respectively. Note that x is in the direction of the bilayer normal.

The total density of lipid chains is calculated as the area per lipid chain, A_L, via

$$A_L = \left(N_\alpha^{-1}\int \rho_\alpha(x)dx\right)^{-1} \tag{3}$$

where N_α is the number of beads of type α on the lipid chain. The surface tension of a given bilayer is

$$\gamma = (\Delta\Omega[\rho_\alpha(\mathbf{r})] - \Delta\Omega^s)/A, \tag{4}$$

where the Δ indicates that free energies are measured relative to a homogeneous mixed lipid-solvent system, Ω is the free energy for the inhomogeneous system containing a bilayer, Ω^s is the free energy of a pure solvent at the density observed far from the bilayer in the inhomogeneous system, and A is the total area.

C. Molecular dynamics simulations

In the MD simulations bonding is enforced with a harmonic bond potential of the form

$$V_{\text{bond},\alpha\beta} = k_b(r - \sigma_{\alpha\beta})^2, \tag{5}$$

where r is the distance between two bonded sites. We set $k_b = 10^3\epsilon\sigma^{-2}$, of the same order of magnitude as used by Goetz and Lipowsky [4]. Because we did not constrain the bond lengths to be rigidly fixed, this model differs slightly from that used in the DFT calculations; however, with the relatively large value of k_b the average bond length is close to the long time average of σ [4].

MD simulations were carried out using the parallel LAMMPS MD code [18], using eight processors on the Sandia Cplant cluster. A time step of 0.005τ (in reduced LJ units) was used. The temperature T was controlled with a Nosé-Hoover thermostat using a coupling frequency of 10 τ^{-1}. Constant-pressure simulations employed an anisotropic Nosé-Hoover barostat which allowed all three box dimensions to fluctuate independently.

We performed two different kinds of simulations. The first set consisted of a liquid of either melt or solvated lipids near surfaces, which were run in the *NVT* ensemble. Initial states for these simulations were prepared by randomly placing lipid molecules and solvent sites in the simulation box, and overlaps were removed using a soft nonbond potential. The systems were equilibrated for typically 3×10^5 time steps, and statistics to obtain smooth density profiles were collected for 10^6 to 1.5×10^6 time steps. The melt lipid-wall systems consisted of 1000 lipid molecules confined between two surfaces as described below, with periodic boundaries in the other two directions. The lipid-solvent-wall systems consisted of 600 lipid molecules and 17 621 solvents for the repulsive systems, and 400 lipid molecules with 11 747 solvents for the attractive systems.

We also simulated solvated lipid bilayers, using periodic boundary conditions. These systems were prepared in two ways. First we verified that our lipid model would self-assemble into a bilayer by starting from random configurations of lipids and solvent. These systems were run in the *NPT* ensemble until a bilayer formed. These bilayers were randomly oriented in the simulation box. To extract density profiles, we created initial configurations consisting of a bilayer oriented parallel to two of the simulation box directions, with the lipids initially packed on a hexagonal lattice. The bilayer was then equilibrated in the *NPT* ensemble for up to 2.5×10^6 time steps until the system reached its equilibrium area per lipid. This approach led to a well-equilibrated bilayer that remained parallel to two of the simulation box directions. We also note that all three box dimensions were independently controlled. The area per lipid was thus controlled by the interactions and not by the initial box size. Furthermore, we kept all three components of the pressure tensor equal ($P_{xx} = P_{yy} = P_{zz}$) so that the surface tension $\gamma=0$ [19]. Results reported for areas per lipid are thus for zero tension bilayers. In order to calculate density profiles, we ran the equilibrated systems in the *NVT* ensemble for 5×10^5 time steps for equilibration, followed by another 8×10^5 time steps to collect statistics. We simulated several different sized systems, consisting of either $n_L=220$ or $n_L=450$ lipid molecules and from 50% to 60% site density of solvent.

III. VERIFYING THE APPROACH

There are several possible sources for error in the DFT approach of paper I. While it is difficult to tease these errors apart to assess them separately, this section explores several example systems to rigorously test the predictions of the DFT in order to determine the net effect of the approximations in studies of lipid bilayers. Briefly, we expect discrepancies could come from the following sources. First, the CMS DFT is based on a second-order expansion of the free energy, and so precludes liquid-vapor or wetting transitions. Second, the hypernetted chain (HNC) form of the mean field used in the CMS DFT is known to overpredict structure in fluids near surfaces. Third, the DFT incorporates liquid state structure from PRISM theory, and so may have errors that propagate from the liquid state calculations. We note that errors due to the HNC field and due to approximations in PRISM theory are known to partially compensate each other [14]. Fourth, attractions are introduced in the DFT calculations via a perturbation approach with an unshifted core term (see Appendix A of paper I). Fifth, the chain statistics are not the same in the simulation and the DFT. This is because the simulations enforce excluded volume, so that the chain statistics are not Gaussian on short length scales. By contrast, in the DFT the chains follow random walks and thus allow chain overlaps (although the repulsive part of the LJ interactions will counter this effect). And finally, while DFT holds bond lengths constant, the MD bonds can fluctuate slightly [see Eq. (5)].

A. Lipids at surfaces

The CMS DFT has not previously been used to our knowledge to treat an asymmetric triblock copolymer such as our model 8-2-8 lipid. As a rigorous test on fluid structure, we performed both density functional and molecular dynamics calculations of the lipid molecules at surfaces. In these calculations, the size asymmetry of the head and tail beads is preserved, but the interactions are all taken to be identical ($\epsilon_{\alpha\beta}=1$, with equal cutoffs r_c for all species). Thus no self-assembly is expected. While previous work found that the CMS DFT with Lennard-Jones interactions was accurate in describing the self-assembly of diblock copolymers, both in the bulk and in thin films [20,21], only symmetric diblocks were studied in those cases. Symmetric diblocks are a special case because while the individual $\rho_\alpha(\mathbf{r})$ show microphase separation, they are decoupled by symmetry from the total density $\Sigma_\alpha\rho_\alpha(\mathbf{r})$ which controls packing effects [21,22]. Thus we anticipate that there may be more interplay between total density and concentration effects in our asymmetric lipid model.

We considered three kinds of surface-lipid systems all at $kT/\epsilon=1.0$. The first case had purely repulsive interactions both between the chains and between the walls and the chains (case RR). Another calculation had attractive interactions between the chains as well as between the surfaces and the chains (case AA). A final calculation had attractive chain-chain interactions, but repulsive chain-wall interactions (case AR). Attractive chain interactions were generated by setting longer LJ cutoffs for the AA and AR cases. Specifically the AR and AA cases had $r_c=3.5\sigma$ while the RR case had $r_c=2^{1/6}\sigma_{\alpha\beta}$. Surface-fluid interactions were a function of the distance x between a given point in the fluid and the surface, and were of an integrated LJ form,

$$V_\alpha(x)=\frac{2\pi\epsilon_{w\alpha}}{3}\left[\frac{2}{15}\left(\frac{\sigma_{w\alpha}^{12}}{x^9}\right)-C\left(\frac{\sigma_{w\alpha}^{6}}{x^3}\right)\right], \tag{6}$$

where $C=0$ for the RR and AR cases while $C=1$ for the AA case. Note that the wall-site interaction parameters were $\epsilon_{w\alpha}=1.0$ and $\sigma_{w\alpha}=1.44$. The bulk density ρ_b in the fluid needed for the DFT calculations was chosen to match the density far from the surfaces in the MD simulations. The bin size for the MD density profiles and the mesh size for DFT calculations were both set to $\Delta x=0.1$.

A comparison of DFT and molecular dynamics calculations is shown in Fig. 1. The DFT reproduces structure reasonably well in both the RR and AA cases. This indicates that the theory is able to handle the packing of the different size sites in the lipid molecule correctly. However, in the AR case, the DFT significantly overpredicts structure at the interface. A similar disagreement has been observed for attractive homopolymers near repulsive surfaces [23]. In that paper, it was shown that an *ad hoc* correction of the repulsive (PRISM) part of the direct correlation functions by a constant factor improved the result. A similar correction is applied in Fig. 1(D) where the agreement is now quite good. However, this correction is completely empirical, and so we do not pursue it further here except to note that the theory may not work well for lipids near strongly solvophobic surfaces.

Figure 2 shows results for a mixture of lipids and solvent next to a surface. Again, all the site-site interactions were identical so that we are again probing the ability of the theory to predict packing. Figure 2 shows the completely repulsive RR case and the completely attractive AA case. In both cases, although the shapes of the density profiles are in agreement with the MD simulations, the DFT predicts a much higher head-group peak near the surface, whereas the MD simulations predict that more of the solvent goes to the surface. The DFT result is somewhat surprising, as one might expect that the lipids could gain more configurational entropy by not being too close to the surface, but putting the solvent there instead. The discrepancy is presumably related to the balance of approximations in the HNC field and the PRISM input, as mentioned above. The agreement is not as good as for the melt of lipids shown in Fig. 1, which must be due to inclusion of the solvent. We examine the quality of

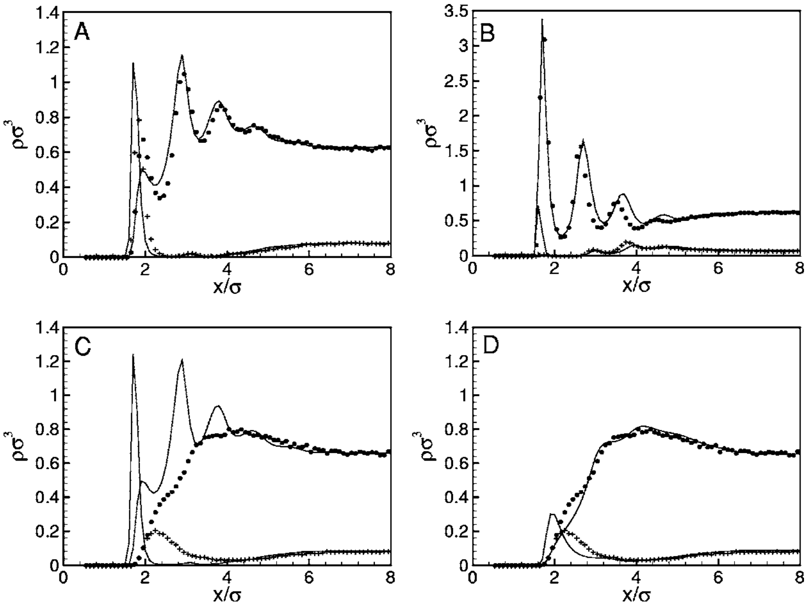

FIG. 1. A comparison of density functional (curves) and molecular dynamics (symbols) calculations on a liquid of model lipids near surfaces. We show density profiles for the head groups (plus signs) and tail beads (circles) near a surface located at $x=0$. The various cases are (A) Repulsive chains at a repulsive wall with a bulk density of $\rho_b\sigma^3=0.711$, (B) attractive chains at an attractive wall with a bulk density of $\rho_b\sigma^3=0.695$, (C) attractive chains at a repulsive wall with $\rho_b\sigma^3=0.746$, and (D) a modified prediction to the attractive chain repulsive wall case where the repulsive part of the direct correlation functions were reduced in magnitude by a factor of 2.5.

our solvent model in the next section. However, we note that in lipid bilayers, the solvent is excluded from the bilayer, and so we expect the quality of the solvent model to be less important for lipid bilayers than it is in the mixtures discussed here.

B. The solvent model

Given the approximations of the DFT detailed above, it is clear that the single site solvent in this theory will not be the same as the LJ fluid used in simulations. This is illustrated in Fig. 3 where we present pressure-density curves for pure solvents at three different temperatures. We calculated the DFT solvent pressure using the contact density $[P/kT=\rho_s(x=0)$ [24]] for this solvent at a hard wall. We find that the pressure is significantly higher in our solvent than it is in a true Lennard-Jones fluid. For liquidlike densities, P is even higher than in a hard-sphere system described by the Carnahan-Starling equation of state. This result was noted previously by Hooper *et al.* for hard-sphere sites, and is due at least in part to errors in the HNC form of the mean field used in the DFT [14,25]. Taking both the absence of the liquid-vapor transition in this DFT, and the high pressures in Fig. 3, one concludes that this model solvent will behave more like a purely repulsive fluid than like a Lennard-Jones fluid.

While these shortcomings of the CMS solvent are no doubt a significant factor in the poorer performance of the CMS DFT in Fig. 2, there are some advantages to using this particular solvent model. First, it is computationally simple to implement. While there are more accurate density functionals available for inhomogeneous Lennard-Jones fluids, it is not *a priori* clear how to couple these to the CMS polymer DFT used here to treat the lipids. Since we are interested in solutions that exhibit microphase separation, and since we

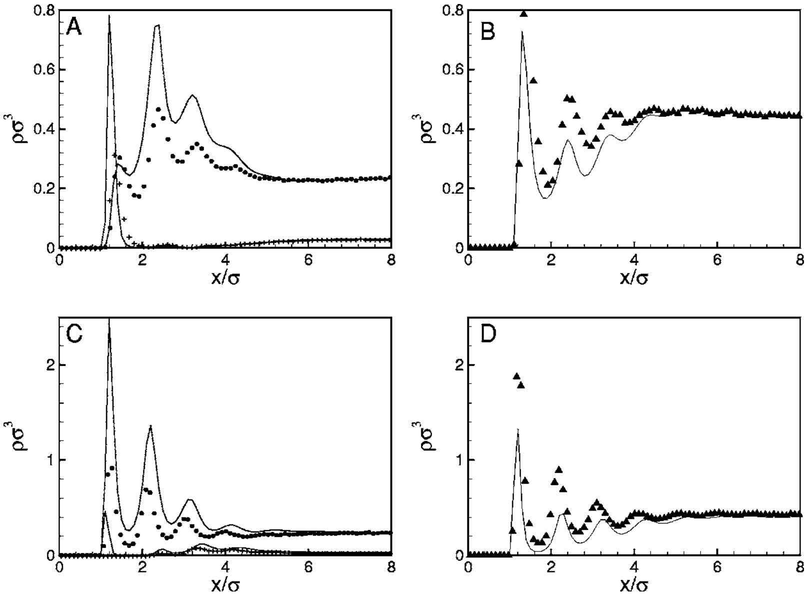

FIG. 2. A comparison of density functional (solid curves) and molecular dynamics (symbols) calculations on solvated lipids near surfaces. The two cases are RR with a bulk density of $\rho_b\sigma^3=0.709$ and a solvent fraction of $x_s=0.630$, showing (A) head groups (solid circles) and tails (plus symbols), and (B) solvent density profiles (triangles); and AA with a bulk density of $\rho_b\sigma^3=0.683$ and solvent fraction $x_s=0.635$, showing (C) head groups (solid circles) and tails (plus symbols), and (D) solvent density profiles (triangles).

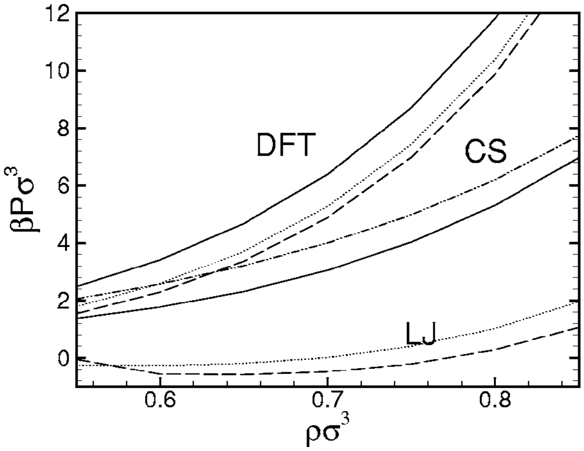

FIG. 3. Pressure as a function of solvent density for three temperatures: $kT/\epsilon=0.85$ (dashed curves), 1.0 (dotted curves), and 2.0 (solid curves). The upper curves are calculated with the current DFT theory, the lower set of curves is from the equation of state for Lennard-Jones fluids determined by simulation [39], and the dash-dotted curve is the Carnahan-Starling (CS) equation of state for hard-sphere fluids [40].

are principally interested in the structure of the lipid rich bilayer phase, a highly accurate solvent treatment may not be required.

IV. STRUCTURE OF LIPID BILAYERS

We now turn to lipid bilayers. It would be reasonable to expect that lipid bilayers based on flexible lipids would exhibit significant interpenetration of the two bilayer leaflets. However, this does not appear to be the case. Figure 4 shows a snapshot of a lipid bilayer at temperature $kT/\epsilon=1$ and a pressure of $P=0.5\epsilon/\sigma^3$ (chosen to approximate atmospheric pressure). The two different leaflets are colored differently, and we see that they only interpenetrate by one or two beads.

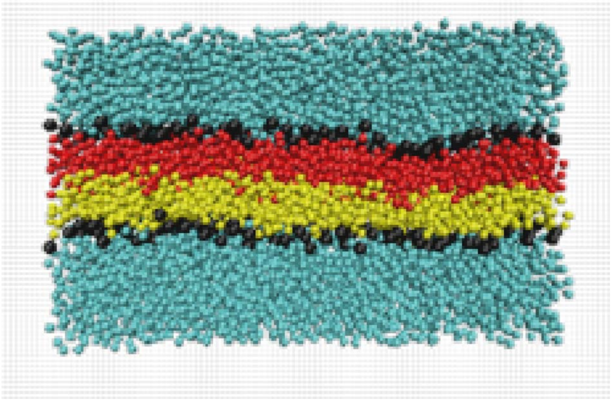

FIG. 4. (Color online) Snapshot of a MD simulation of a solvated lipid bilayer at $kT/\epsilon=1.0$ and $P=0.5\epsilon/\sigma^3$, with $n_L=220$. The large blue (dark) spheres are the head groups, and the smaller cyan (gray) spheres on the outside of the bilayer are the solvent. The lipid tails have been colored according to which leaflet they belong to; upper (red or dark gray) and lower (yellow or light gray) leaflets of the bilayer only interpenetrate over a small distance in the center of the bilayer.

For bilayers, attractive interactions drive the self-assembly, creating fluid interfaces rather than rigid ones. The fluid nature of the interface presents a challenge for comparing DFT- and MD-generated results explicitly. Specifically, the MD simulations exhibit both small scale density fluctuations and long range interface fluctuations of the bilayer. As a result a simple binning of the computational domain to calculate density profiles necessarily results in structures that are more broad than those found in the mean-field DFT.

In order to compare density profiles, we have attempted to correct for the MD interface fluctuations by averaging density profiles locally based on the center of mass of the bilayer at a given position (y,z) in space. (Note that x is taken to be the direction perpendicular to the bilayer-water interface.) The correction was made as follows. For each tail bead, we find all the head groups in a cylinder of radius R_{cyl} parallel to the x axis and centered on the tail bead. We average the x positions of the head groups on each side of the bilayer in this cylinder to produce an average x position x_{top} for the top leaflet and x_{bot} for the bottom leaflet of the bilayer, and use these to find the midpoint of the bilayer as $x_{mid}=0.5(x_{top}+x_{bot})$. The x position of the tail bead is then corrected by the difference between x_{mid} and the actual midpoint of the simulation box. An identical correction is done for all the solvent molecules. The head-group beads are corrected by the same factor as the tail beads to which they are bonded. This correction procedure is analogous to fitting a surface over the fluctuating bilayer and then correcting that surface to be flat, and is similar to a method used previously [6].

We tried several values of the radius of the averaging cylinder. We need R_{cyl} to be large enough to contain enough head groups for good statistics, while still being significantly smaller than the average spatial extent of the interface fluctuations. We found $2 \leqslant R_{cyl} \leqslant 4$ to give indistinguishable results. A comparison of uncorrected and locally averaged MD density profiles is shown in Fig. 5 for two temperatures, $kT/\epsilon=1$ and 1.3. The local averaging sharpens the density profile of the head groups and the interface between the lipids and the solvent considerably, and narrows the density profile of the tail beads slightly as well. In addition, there is an apparent depletion of tail beads in the center of the bilayer that is not obvious if bilayer midpoint corrections are not applied.

Since DFT and MD calculations are done in different ensembles, it is necessary to establish a strategy for mapping between ensembles. If the theory were exact we would expect all possible mapplings to yield identical results; however this is not the case. While temperature can be set identically for both calculations, the remaining two state variables (ρ_b and x_s in the DFT calculations) are set based on observables from MD simulations. Many observables could be used, but we consider (1) the solvent density far from the bilayer, (2) the constraint of zero surface tension, and (3) the observed A_L in the MD bilayer simulations in Fig. 5.

Figure 6 provides the data used to identify the DFT state points that correspond most closely with the MD profiles in Fig. 5. Beginning with the solvent density, in the MD simulations we found that far from the bilayer $\rho_s\sigma^3=0.74$ at $kT/\epsilon=1.0$, and $\rho_s\sigma^3=0.61$ at $kT/\epsilon=1.3$. Figures 6(A) and

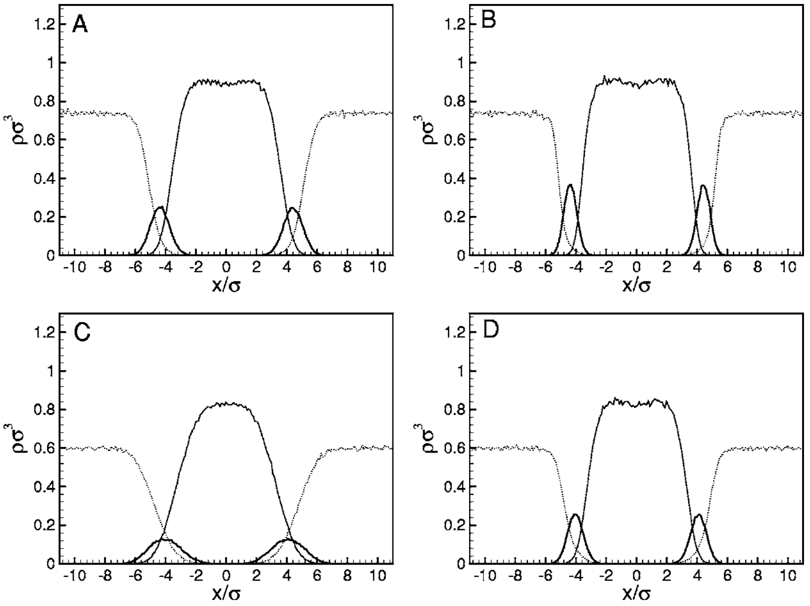

FIG. 5. Density profiles from two MD simulations. Both were run at $P\sigma^3/\epsilon=0.5$, but the first (A) and (B) was run at $kT/\epsilon=1.0$ while the second (C) and (D) was run at $kT/\epsilon=1.3$. Both (A) and (C) show density profiles calculated by straightforward binning. (B) and (D) show profiles in which bilayer midpoint corrections have been applied. In all profiles, the tail beads are shown in solid lines, the head groups are shown in bold lines, and the solvent is shown in a dotted line.

6(B) show DFT predictions for the variation of the solvent density far from the bilayer as a function of ρ_b, x_s, and T. Since the solvent density is relatively insensitive to x_s at least over the range $0.2<x_s<0.8$, we use the data in Fig. 6(A) to set $\rho_b\sigma^3=0.68$ for $kT/\epsilon=1.0$, and $\rho_b\sigma^3=0.59$ for $kT/\epsilon=1.3$.

Figure 6(C) shows DFT calculations of the area per lipid as a function of x_s while holding $\{\rho_b\sigma^3=0.68,\ T=1.0\}$ or $\{\rho_b\sigma^3=0.59,\ T=1.3\}$ constant. The MD simulations had $A_L=5.1\sigma^2$ at $kT/\epsilon=1$ and $A_L=6.2\sigma^2$ at $kT/\epsilon=1.3$. To match these values, Fig. 6(C) can be used to identify $x_s=0.392$ and 0.364 for $kT/\epsilon=1.0$ and 1.3 respectively.

If we choose instead to constrain the solvent densities to the MD values and the surface tension to zero, the two state points are found to be $\{x_s=0.442,\ \rho_b\sigma^3=0.68,\ kT/\epsilon=1\}$ and $\{x_s=0.415,\ \rho_b\sigma^3=0.59,\ kT/\epsilon=1.3\}$. Paper I discusses the identification of zero tension bilayers; we just note here that there is only one zero tension point in a fixed $\{\rho_b,T\}$ slice of the phase space.

Finally, Fig. 6(D) shows the area per lipid as a function of ρ_b for zero tension bilayers at $kT/\epsilon=1.3$. This figure shows that the DFT cannot predict areas per lipid as large as those observed in zero tension MD bilayers. This may be a consequence of the high solvent pressures in this theory. Therefore, it is not possible to use $\gamma=0$ and A_L as simultaneous constraints on the mapping of ensembles. However we note that in designing DFT approaches for bilayers, achieving this mapping would be optimal.

Figure 7 shows DFT predictions for the bilayers using the $\{\rho_s,A_L\}$ and $\{\rho_s,\gamma=0\}$ constraints to determine state points as detailed above. These structures should be compared to the MD results in Fig. 5. Overall the agreement is quite good. The basic structure of the bilayer (tails to the center, head groups at the interface, solvent excluded) is found by both methods. The magnitudes of the density profiles are similar as well, and both calculations predict fluid bilayers. However, there are some notable differences. The DFT predicts

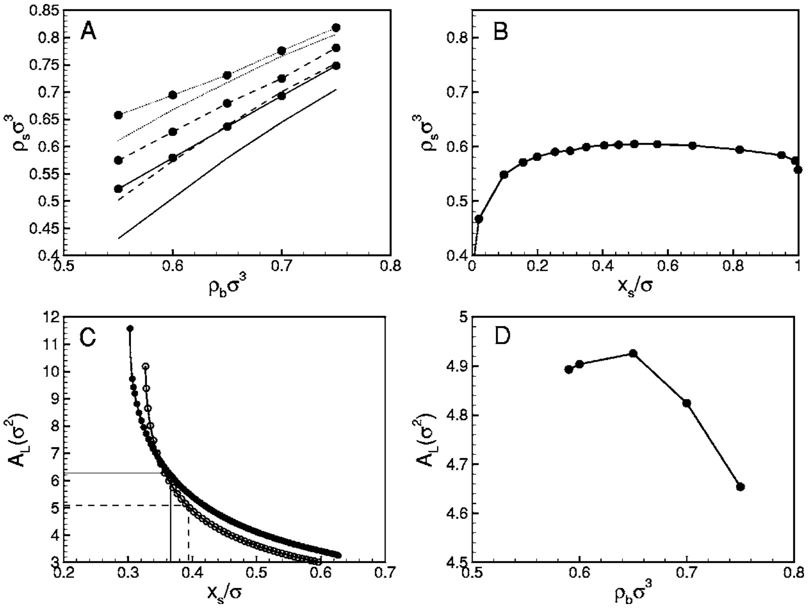

FIG. 6. Data used to pin the DFT ensemble in order to compare with MD simulations on lipid bilayers. (A) shows the relationship between observed solvent density far from the bilayer and total density in the bulk fluid for $kT/\epsilon=0.9$ (dotted lines), 1.3 (dashed lines), and 2.5 (solid lines) at both $x_s=0.1$ (no symbols) and $x_s=0.5$ (with symbols). (B) shows the variation of the solvent density with x_s for the particular case of $\rho_b\sigma^3=0.59$ and $kT/\epsilon=1.3$, (C) shows the relationship between the area per lipid molecule in the bilayer and the chemical potential variable x_s at the two state points $\{kT/\epsilon=1.3,\rho_b\sigma^3=0.59\}$ (open circles) and $\{kT/\epsilon=1.0,\rho_b\sigma^3=0.68\}$ (closed circles), and (D) shows the area per lipid molecule measured at the point of zero surface tension varying with total bulk density $\rho_b\sigma^3$, when the temperature is held constant at $kT/\epsilon=1.3$.

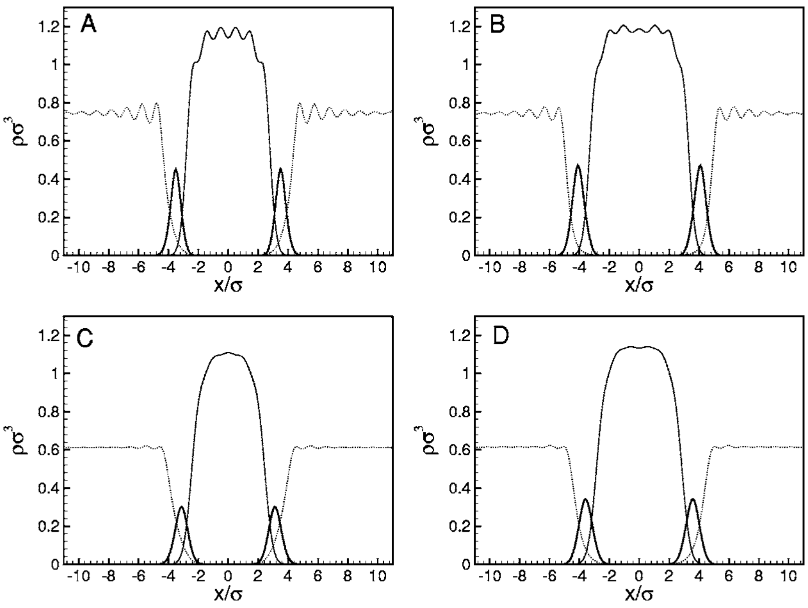

FIG. 7. DFT predictions for lipid bilayer profiles for comparison with MD predictions in Figs. 5(B) and 5(D). (A) and (B) show results for $kT/\epsilon=1.0$ while (C) and (D) show results for $kT/\epsilon=1.3$. The DFT state points for (A) and (C) were set based on matching solvent density far from the bilayer and area per lipid in the observed bilayer. The state points for (B) and (D) were chosen by matching the solvent density and requiring the bilayer to be at zero surface tension.

bilayers that are slightly narrower with a higher tail peak density and some additional structure in the center of the bilayer. These DFT profiles do not have the depletion of tails observed in the center of mass corrected MD profiles, although such features are predicted at other state points [see Figs. 2 and 4(B) of paper I]. We expect that an improved solvent model would have lower pressure at a given bulk density, and would likely result in bilayers with larger A_L.

For more detail on the structure, we compare the densities of the ends of the lipid tails in the two approaches. The MD snapshot shown in Fig. 4 implies that there is only a small amount of interpenetration of the two leaflets in the bilayer. We infer a similar result for the DFT bilayers based on the density profiles for the last site in the lipid tails, shown in Fig. 8(A). We see that the end densities are qualitatively similar in the DFT and MD profiles. In particular, there is very little overlap in the distributions of the ends of the tails and the head groups. This implies that the leaflets cannot be fully interdigitated.

Further evidence for this picture is shown in Fig. 8(B) where we plot the site density distribution for each of the sites on the chain from the DFT calculations. Note that the chain is symmetric, and these site densities include contributions from each pair of identical beads (in the two tails). This figure shows that while the density distributions for beads 1–3 are overlapping with a single peak in the center of the bilayer, beads 4–8 each have a distinct peak getting nearer to the head groups. Thus, the bilayer is most mixed in the center, with overlap of the leaflets most likely between the three end beads of the lipids on opposing monolayers.

In Fig. 9 we show both the area per lipid and the thickness of the bilayer as a function of temperature. DFT data along the zero tension line as well as along the single bilayer turning points, which define the limits of stability of the isolated bilayer, are included in the plots. (See Appendix B of paper I for a description of turning points.) As the bilayer thickness increases, the area per lipid decreases. For the physically realistic system along the $\gamma=0$ line, the area per lipid decreases roughly linearly with temperature in both the DFT and MD cases, in agreement with experiment [26] and previous simulations [8]. Given the approximations of the

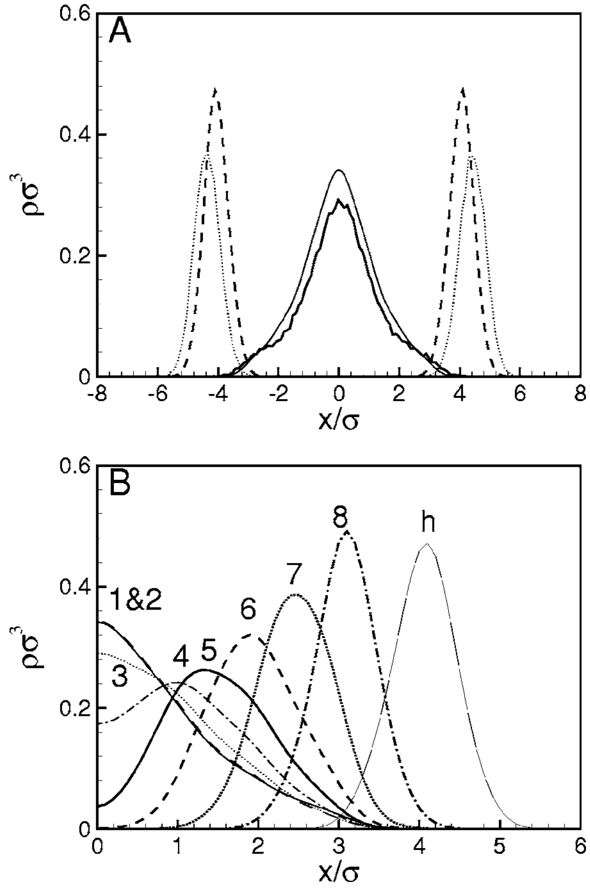

FIG. 8. Site density distributions in zero tension bilayers at $kT/\epsilon=1.0$. (A) compares the end site density distribution from MD (thick solid curve) and DFT (thin solid curve), as well as the head group densities from MD (dotted curves) and DFT (dashed curves). (B) shows DFT predictions for all the different sites on the lipid, as labeled. In both cases, the center of the bilayer is found at $x/\sigma=0$.

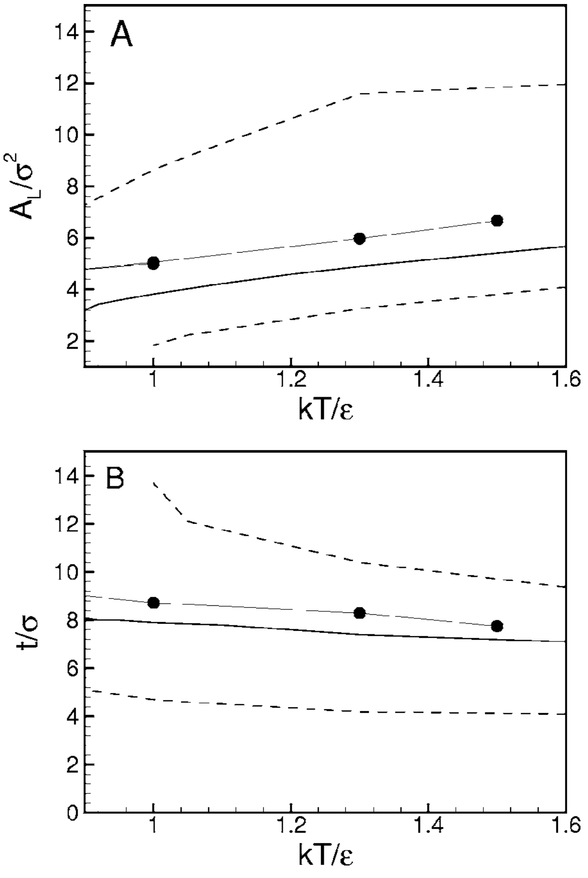

FIG. 9. Bilayer properties for the coarse-grained lipid models: (A) the area per lipid, and (B) the bilayer thickness. Dashed lines show DFT bilayer properties on the turning points (the limits of stability of the isolated bilayer), while the solid line shows the DFT data along the $\gamma=0$ line. The MD simulations, shown in the filled circles, were performed for systems with $n_L=450$ and at a pressure of $P\sigma^3/\epsilon=0.5$, for which γ is close to zero.

model, the agreement of the $\gamma=0$ DFT bilayer properties with MD are quite good.

On decreasing temperature below about $kT/\epsilon=0.95$, the DFT predicts ordered bilayers (see paper I). The transition from the fluid bilayer phase to the ordered bilayer phase was continuous, and there were first order phase transitions between ordered bilayers with different numbers of density peaks in the tail region. We looked for these ordered bilayers in our MD simulations, but did not find them. Instead, we found that as we lowered temperature the solvent eventually froze into a crystal while the lipid bilayer remained disordered and fluid.

In order to assess the impact of the approximate solvent model, we ran MD simulations with purely repulsive interactions for the solvent, at an external pressure of $P=4\epsilon/\sigma^3$. At $kT/\epsilon=0.6$, there was a small amount of ordering in the tails, with nine peaks of amplitude $\approx 0.2\rho\sigma^3$ in the tail densities. However, this case still had a fairly liquidlike area per lipid of $A_L=3.75\sigma^2$.

Finally, we also performed a simulation on one of the stiff eight-bead tail lipids from Ref. [8]. We started the system in the gel phase at $kT/\epsilon=1.05$ and then turned off the angle potential between beads. The bilayer melted. We then began again in the gel phase, lowered the temperature in the gel phase to $kT/\epsilon=0.75$ and then turned off the angle potentials; we again found that the bilayer melted into a fluid phase. This is clearly seen in the area per lipid; for the stiff lipids in the gel phase at $kT/\epsilon=0.75$ the area per lipid is $A_L=2.30\sigma^2$ whereas for the flexible lipids at the same conditions we find $A_L=3.87\sigma^2$.

Thus, it seems that the flexible lipid tails preclude a gel transition in the MD simulations. In comparing ordered DFT predictions with ordered bilayers based on stiff lipids, we find that ordering in DFT occurs in the same range of temperatures and ordered bilayers have similar A_L as in previously published MD simulations of the gel phase [8]. However, the stiff lipid MD simulations had bilayers with well separated leaflets where the number of observed density peaks in the tail region was the same as the number of tail beads from the end to the head group. We never observed fully separated leaflets with 16 peaks in the DFT calculations. Thus while ordering is an important feature of lipid bilayers, flexible chain models are likely not optimal for futher investigations of ordered states.

V. MECHANICAL PROPERTIES OF LIPID BILAYERS

In this section we compare two fundamental mechanical properties of the fluid bilayers as obtained from the DFT and the MD simulations, namely, the lateral stress profiles and the area compressibility modulus. Other important elastic constants of bilayer membranes include the bending modulus κ and the splay modulus $\bar{\kappa}$. These moduli are related to the lateral pressure profiles, but to calculate them from our DFT would require solutions in curved geometries [27,28], which is beyond the scope of this paper.

A. Lateral stress profiles

As described in paper I, the surface tension across the entire bilayer is given by

$$\gamma = \int_{-\infty}^{\infty} dx\, s(x) = \int_{-\infty}^{\infty} dx [P_N(x) - P_T(x)], \tag{7}$$

where the stress profile is $s(x)=P_N(x)-P_T(x)$, x is the direction normal to the bilayer, $P_N(x)$ is the normal component of the pressure tensor (a constant for all x as it must be for mechanical equilibrium), and $P_T(x)$ is the tangential component of the pressure tensor. The stress profile itself [or the lateral pressure profile, $\pi(x)=-s(x)$] is a quantity of considerable interest because it is related to the curvature elasticity of the membrane [27,28]. Furthermore, changes in lateral stress in, e.g., mixed lipid bilayers affect membrane protein conformational changes and activity [29,30].

However, the lateral pressure $P_T(x)$ and hence the stress tensor $s(x)$ are not uniquely defined, as shown by Schofield and Henderson [31]. We can see this by noting the virial expression for the pressure tensor **P**:

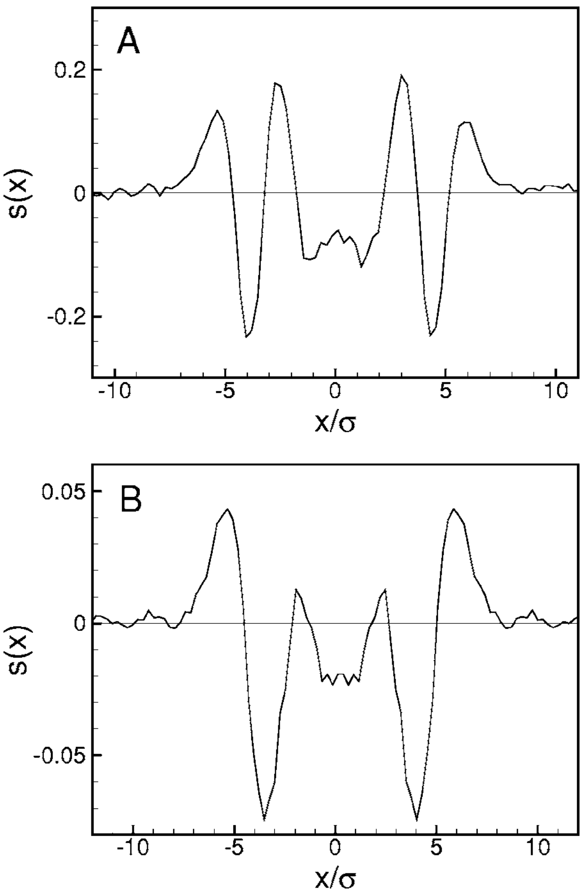

FIG. 10. Stress profiles calculated from a MD simulation of 220 lipids at $P\sigma^3/\epsilon=0.5$ and (A) 1 and (B) 1.3. The profile in (B) was averaged about the middle of the bilayer.

$$\mathbf{P}V = NkT\mathbf{I} + \frac{1}{2}\sum_{i=1}^{N}\sum_{j=1}^{N}\langle \mathbf{f}_{ij}\mathbf{r}_{ij}\rangle \tag{8}$$

where N is the number of particles, $\mathbf{I}$ is the unit tensor, and $\mathbf{f}_{ij}$ is the force between particles i and j separated by the vector $\mathbf{r}_{ij}$. The first term above is the kinetic contribution and the second is the interaction contribution. The nonuniqueness of $\mathbf{P}$ arises because the path between particles is not specified. The surface tension γ is invariant with respect to the choice of path, but $\mathbf{P}$ is not [31]. Choosing a straight line between particles i and j leads to the Irving-Kirkwood (IK) expression for the pressure [32], which we will use here in computing $P_T(x)$ from our MD results. However, other choices of path are possible.

We calculate the components of the IK pressure tensor directly in the MD simulations, using the expressions derived by Goetz and Lipowsky [4] to include the many-body terms in the interaction potentials. The Hardy method [33] is used to bin the stress into slices perpendicular to the x axis and to determine the contours between pairs of sites. Because $s(x)$ fluctuates considerably, we calculated it using the small system of 220 lipids, at $kT/\epsilon=1.0$ and 1.3, averaging over 10^7 and 3×10^7 time steps, respectively. The resulting MD stress profiles are shown in Fig. 10. We find by integration of $s(x)$ that the surface tension is essentially zero, $\gamma=-0.037\epsilon/\sigma^2$, for $kT/\epsilon=1$. For the higher temperature of $kT/\epsilon=1.3$ we find $\gamma=-0.110\epsilon/\sigma^2$, so that in this case the bilayer is under a small compression. We note that the stress profiles look very similar to that for a bilayer of more stiff coarse-grained lipids obtained by Goetz and Lipowsky [4]. They considered a coarse-grained lipid with four tail beads per tail and angle potentials between all sites so that the tails were semiflexible (they preferred to be straight). For both lipid models, one finds a total stress profile with several different peaks. The physics underlying the spatial variations in $s(x)$ is fairly clear. As it must be, the total stress is zero in the solvent region, and reaches a peak at the solvent (S)–head group (H) interface corresponding to the SH interfacial tension. The adjacent negative (compressive) region is associated with the attractive HH potential, and is followed by a second peak at the head group (H)–tail (T) interface corresponding to the HT interfacial tension. The stress profile in the center of the bilayer tail region is negative, corresponding to a compression of the tails.

We note that we only expect $s(x)$ to be nonunique on a length scale of the order of the range of the interparticle interactions. In this work the largest cutoff was 3.5σ, clearly much shorter than the total thickness of the lipid bilayer. Variations in $s(x)$ on length scales longer than this should thus be unique. In atomistic simulations of lipid bilayers, the typical cutoffs for LJ interactions (10–12 Å) are a smaller proportion of typical bilayer thicknesses (e.g., 60 Å or so) than in this work; thus lateral pressure profiles calculated in atomistic simulations may be even more physically meaningful than those calculated here. Some (IK) lateral pressure profiles from atomistic simulations have been published recently in the literature, and show some of the same qualitative features as the coarse-grained models [34,35].

The stress profile can also be calculated using the DFT from the excess surface free energy, as discussed in paper I. This calculation identifies the surface excess grand free energy density directly with the stress profile. Due to the nonuniqueness of $s(x)$, it is not *a priori* clear that this stress profile will be the same as the IK stress profile derived from the virial route. However, previous work on mean-field theories found that the same physics applied to the spatial behavior of $P_T(x)$ calculated from the energetic and virial routes [36]. We find that this is also the case here.

Figure 11 shows stress profiles calculated from Eq. (A10) in paper I and shifted by a constant so that $s(x)=0$ in the bulk solvent region. The overall shape of the stress profiles is quite similar to the MD case, with the same number of major peaks. There is more structure in the profile at $kT/\epsilon=1.0$, corresponding to the additional order in the bilayer itself as seen in Figs. 7(A) and 7(B). In both methods the magnitudes of the peaks decrease with increasing temperature. For example, for the head groups the height of the peak in $s(x)$ decreases by a factor of 3.3 for the MD and 3.0 for the DFT calculations on going from $kT/\epsilon=1.0$ to $kT/\epsilon=1.3$. However, the magnitudes of the stress are much larger in the DFT than in the MD. In part this is related to the higher densities of the lipids in the DFT density profiles as compared to the corresponding MD calculations (see Fig. 7). We also note

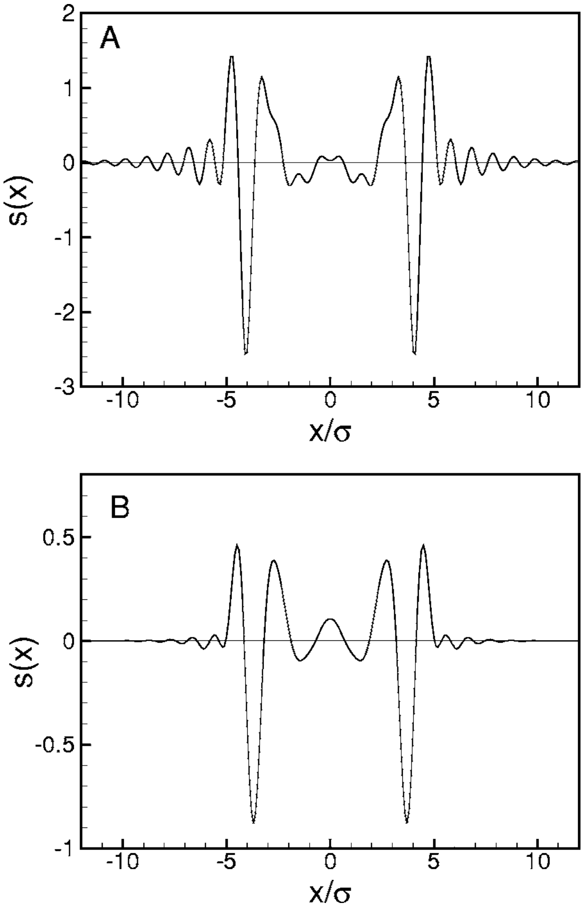

FIG. 11. Stress profiles calculated from DFT calculations at (A) $\{kT/\epsilon=1,\rho_b\sigma^3=0.68,\gamma=0\}$ and (B) $\{kT/\epsilon=1.3,\rho_b\sigma^3=0.59,\gamma=0\}$, corresponding to the same state points as Fig. 7.

that no bilayer midpoint corrections were applied in the MD calculation of the stress profiles, so these must be broadened by transverse fluctuations of the bilayer. From Fig. 7 we see that the broadening effect in the density profiles reduces, for example, the head-group density peaks by factors of about 1.5 and 2 for $kT/\epsilon=1.0$ and $kT/\epsilon=1.3$, respectively. Thus some of the difference in the results is due to interface fluctuations.

Several previous authors have also calculated lateral stress profiles from mean-field theories of lipid bilayers [29,37,38]. All of these theories have assumed that the lipid tails form an incompressible liquid, and furthermore they calculate only the contribution of the tails to the lateral pressure profile. The general result is that there is a peak in the lateral pressure $\pi(x)$ in the middle of each leaflet of the bilayer, with the lateral pressure falling in the middle of the bilayer and near the tail-head interface. Recalling that $\pi(x)=-s(x)$, this is also what we see in the tail region of the bilayer. In previous work the lateral pressure is positive (and thus the stress profile is negative) throughout the tail region, as it must be since it is calculated as the constraint which must be applied to impose incompressibility and thus a constant density through the tail region. In contrast, we find that the peak in $s(x)$ in the tail region in the DFT goes above zero for $kT/\epsilon=1.3$, indicating that the ends of the tails are under tension in our model for this state point.

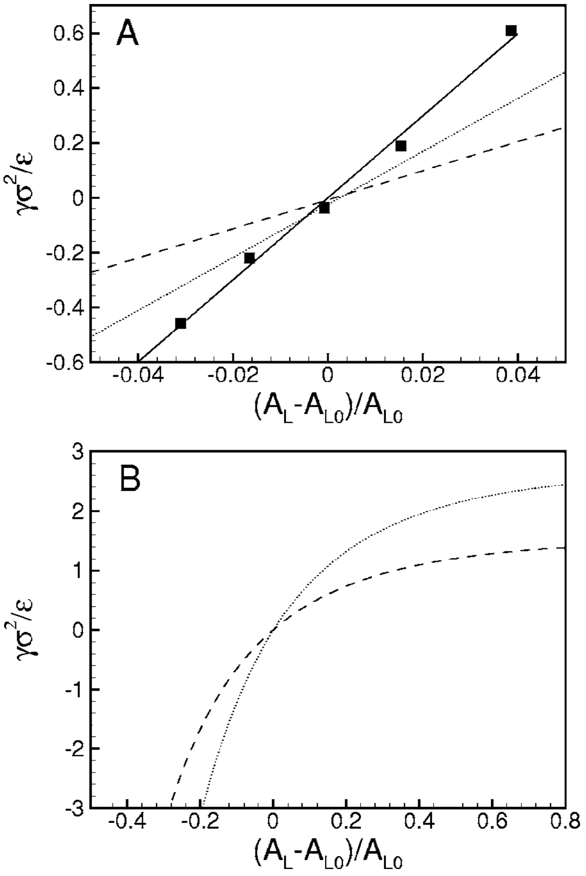

FIG. 12. Surface tension as a function of area per lipid, relative to the zero tension area per lipid. (A) MD results for $kT/\epsilon=1.0$ (square symbols with best linear fit) and DFT results for $kT/\epsilon=1.0$ (dotted line) and $kT/\epsilon=1.3$ (dashed line), corresponding to the same state points as Fig. 7. (B) shows the full nonlinear behavior of the DFT results over a wider range of $(A_L-A_{L0})/A_{L0}$.

B. Area compressibility

A final quantity that is straightforward to compare is the area compressibility modulus K_A of the membrane. This modulus can be obtained from the dependence of the surface tension on the area per lipid near the zero tension point,

$$\gamma \approx K_A(A_L-A_{L0})/A_{L0}, \tag{9}$$

for small deviations of A_L from its value A_{L0} at $\gamma=0$.

We performed several MD simulations at $kT/\epsilon=1$ and at constant area and constant normal pressure $P_N\sigma^3/\epsilon=0.5$ to obtain K_A from the variation of γ with A_L. The results are shown in Fig. 12(A). From the linear fit we obtain $K_A=15.2\epsilon/\sigma^2$. This value is comparable with previous results from coarse-grained MD simulations. Goetz and Lipowsky [4] obtained $K_A=14.3\epsilon/\sigma^2$ at $kT/\epsilon=1.35$ for their stiff, four-bead tail lipid. Using a similar model, Stevens [8] found a value of $K_A=9.4\epsilon/\sigma^2$ for lipids with six-bead tails at $kT/\epsilon=1.05$.

For the DFT calculations, we note that the solvent density far from the bilayer is nearly constant as we change the area per lipid by changing x_s, as shown in Fig. 6(B). Thus, $\gamma(A_L)$ can be obtained simply from the arclength continuations done at constant temperature in paper I. The results for two different temperatures in the linear region around $\gamma=0$ are also shown in Fig. 12(A). For larger magnitudes of γ the curves become nonlinear and saturate at large values of A_L as shown in Fig. 12(B), a result found previously [4,6]. We find that $K_A=9.72\epsilon/\sigma^2$ for $kT/\epsilon=1.0$ and $K_A=5.31\epsilon/\sigma^2$ for $kT/\epsilon=1.3$. As expected, the compressibility is lower (higher modulus) at lower temperatures. The DFT is more compressible than the MD calculation, but is of the same order of magnitude. Because the DFT does not strictly enforce excluded volume in the chain configurations, we would expect it to yield a somewhat more compressible bilayer.

VI. SUMMARY

We have compared results of CMS DFT and MD calculations for a freely jointed coarse-grained model of lipids. The MD simulations showed that these flexible model lipids will self-assemble into a bilayer, and that the two leaflets of the bilayer are only slightly interdigitated. Comparisons of DFT calculations and MD simulations of lipids near surfaces demonstrated that the theory predicts packing in these asymmetric molecules rather well. Our single site solvent model is somewhat different from the LJ fluid used in the simulations, but is nevertheless simple to use.

We are able to obtain fluid bilayer solutions of the DFT which are quite similar to the corresponding MD bilayer profiles, once those profiles have been corrected for transverse fluctuations of the bilayer. We did not find an ordered or gel phase in the MD simulations, although ordered phases are predicted by the DFT; thus the theory does not compare well with simulation at low temperatures. However, the physical properties of the fluid bilayers are also similar in the DFT and MD calculations, and they do exhibit the same trends with temperature. Calculation of the lateral stress profile is particularly straightforward with the DFT and gives similar shapes as the Irving-Kirkwood stress profiles calculated with MD. We also showed that the area compressibility modulus compares favorably between the DFT and MD calculations, although the DFT system is somewhat more compressible. The DFT thus provides an attractive way to calculate mechanical properties of more complex systems such as mixed lipid bilayers or assemblies of proteins and lipids.

ACKNOWLEDGMENTS

We thank John Curro, John McCoy, and Mark Stevens for helpful discussions, and Mark Stevens for assistance with the MD simulations. A.L.F. also thanks the Isaac Newton Institute for Mathematical Sciences at the University of Cambridge for its hospitality, where some of this work was performed. Sandia is a multiprogram laboratory operated by Sandia Corporation, a Lockheed Martin Company, for the United States Department of Energy under Contract No. DE-AC04-94AL85000. This work has been supported by the Sandia LDRD program.

---

[1] M. Müller, K. Katsov, and M. Schick, J. Polym. Sci., Part B: Polym. Phys. **41**, 1441 (2003).

[2] J. C. Shelley, M. Y. Shelley, R. C. Reeder, S. Bandyopadhyay, and M. L. Klein, J. Phys. Chem. B **105**, 4464 (2001).

[3] S. J. Marrink, A. H. de Vries, and A. E. Mark, J. Phys. Chem. B **108**, 750 (2004).

[4] R. Goetz and R. Lipowsky, J. Chem. Phys. **108**, 7397 (1998).

[5] R. Goetz, G. Gompper, and R. Lipowsky, Phys. Rev. Lett. **82**, 221 (1999).

[6] J. C. Shillcock and R. Lipowsky, J. Chem. Phys. **117**, 5048 (2002).

[7] M. J. Stevens, J. H. Hoh, and T. B. Woolf, Phys. Rev. Lett. **91**, 188102 (2003).

[8] M. J. Stevens, J. Chem. Phys. **121**, 11942 (2004).

[9] L. J. D. Frink and A. L. Frischknecht, preceding paper, Phys. Rev. E **72**, 041923 (2005).

[10] D. Chandler, J. D. McCoy, and S. J. Singer, J. Chem. Phys. **85**, 5971 (1986).

[11] D. Chandler, J. D. McCoy, and S. J. Singer, J. Chem. Phys. **85**, 5977 (1986).

[12] J. D. McCoy, S. J. Singer, and D. Chandler, J. Chem. Phys. **87**, 4853 (1987).

[13] J. B. Hooper, J. D. McCoy, and J. D. Curro, J. Chem. Phys. **112**, 3090 (2000).

[14] J. B. Hooper, M. T. Pileggi, J. D. McCoy, J. D. Curro, and J. D. Weinhold, J. Chem. Phys. **112**, 3094 (2000).

[15] J. B. Hooper, J. D. McCoy, J. D. Curro, and F. van Swol, J. Chem. Phys. **113**, 2021 (2000).

[16] K. S. Schweizer and J. G. Curro, Adv. Polym. Sci. **116**, 319 (1994).

[17] K. S. Schweizer and J. G. Curro, Adv. Chem. Phys. **98**, 1 (1997).

[18] S. J. Plimpton, J. Comput. Phys. **117**, 1 (1995); www.cs.sandia.gov/sjplimp/lammps.html

[19] R. M. Venable, B. R. Brooks, and R. W. Pastor, J. Chem. Phys. **112**, 4822 (2000).

[20] S. K. Nath, J. D. McCoy, J. D. Curro, and R. S. Saunders, J. Chem. Phys. **106**, 1950 (1997).

[21] A. L. Frischknecht, J. G. Curro, and L. J. D. Frink, J. Chem. Phys. **117**, 10398 (2002).

[22] E. F. David and K. S. Schweizer, J. Chem. Phys. **100**, 7767 (1994).

[23] A. L. Frischknecht and J. G. Curro, J. Chem. Phys. **121**, 2788 (2004).

[24] R. Evans, in *Fundamentals of Inhomogeneous Fluids*, edited by D. Henderson (Dekker, New York, 1992).

[25] We note that if one employs the WCA approximation for the potential instead of the approximation in Eq. (A10) of paper I, the pressure at $kT/\epsilon=1$ predicted by the DFT is lowered so that the curve crosses the Carnahan-Starling curve near $\rho_s\sigma^3=0.7$ rather than near $\rho_s\sigma^3=0.6$, but the overall shape of the curve remains similar.

[26] H. Petrache, S. Dodd, and M. Brown, Biophys. J. **79**, 3172 (2000).

[27] S. A. Safran, *Statistical Thermodynamics of Surfaces, Interfaces, and Membranes* (Addison-Wesley, Reading, MA, 1994).

[28] S. M. Oversteegen, P. A. Barneveld, J. van Male, F. A. M. Leermakers, and J. Lyklema, Phys. Chem. Chem. Phys. **1**, 4987 (1999).

[29] R. S. Cantor, Biophys. J. **76**, 2625 (1999).

[30] G. S. Attard, R. H. Templer, W. S. Smith, A. N. Hunt, and S. Jackowski, Proc. Natl. Acad. Sci. U.S.A. **97**, 9032 (2000).

[31] O. Schofield and J. R. Henderson, Proc. R. Soc. London, Ser. A **379**, 231 (1982).

[32] J. H. Irving and J. G. Kirkwood, J. Chem. Phys. **18**, 817 (1950).

[33] R. J. Hardy, J. Chem. Phys. **76**, 622 (1982).

[34] E. Lindahl and O. Edholm, J. Chem. Phys. **113**, 3882 (2000).

[35] J. Gullingsrud and K. Schulten, Biophys. J. **86**, 3496 (2004).

[36] S. M. Oversteegen, P. A. Barneveld, F. A. M. Leermakers, and J. Lyklema, Langmuir **15**, 8609 (1999).

[37] I. Szleifer, D. Kramer, A. Ben-Shaul, W. M. Gelbart, and S. Safran, J. Chem. Phys. **92**, 6800 (1990).

[38] D. Harries and A. Ben-Shaul, J. Chem. Phys. **106**, 1609 (1997).

[39] J. K. Johnson, J. A. Zollweg, and K. E. Gubbins, Mol. Phys. **78**, 591 (1993).

[40] J.-P. Hansen and I. R. McDonald, *Theory of Simple Liquids*, 2nd ed. (Academic Press, San Diego, CA, 1986).